CHAPTER 3

PRELIMINARY INVESTIGATION OF TYPE 446 STAINLESS STEEL

3.1 INTRODUCTION

This chapter provides a description of the suitable composition of ferritic steel. As a potential material for heat exchangers application, there is little information in the literature for Type 446 stainless steel. The microstructure and effect of solution treatment on mechanical properties of Type 446 stainless steel are explored. It is further substantiated with CCT and TTT curve plotted using JMat Pro. The phases available in as-received materials and change in phase after solution treatment are brought to attention using XRD and TEM. The hardness of the solution treated samples and the high temperature tensile test is also carried out to explain the properties of the material at elevated temperature.

3.2 MATERIALS CHARACTERIZATION

3.2.1 Microstructure

The microstructure of the present material is composed of Chromium-rich alpha (α) solid solution with finely divided chromium carbides as shown in optical micrographs and SEM micrograph (Fig 3.1(a)) and (Fig 3.1(c)) respectively. Polygonal grains of the order of 30-70 μm are seen with sharp grain boundaries. However, some grain boundaries may not be resolved, and thus estimation may be on the higher side. The presence of precipitate within the ferritic structure of Type 446 stainless steel has been established [151]. The formation of the precipitate is seen at both grain boundaries as well as the

grain body. The morphology of these precipitates is different. Some are cuboid and near cuboid-shaped of nearly ~1 μm and some are the irregular and elongated shape of ~2-3 μm long. When normalized at 650˚C, no significant change is observed. While at 950˚C treatment, the density of precipitate is seen to be reduced, therefore, it is inferred that the dissolution of these precipitates starts at ~1000˚C. With further increase in temperature up to 1200˚C, grains are observed to be polygonal with sharp grain boundaries and the same size, but precipitation is not seen, i.e., precipitates are dissolved. This may be due to quenching effects where the kinetics of precipitation is not fast, and therefore no precipitate is further seen.
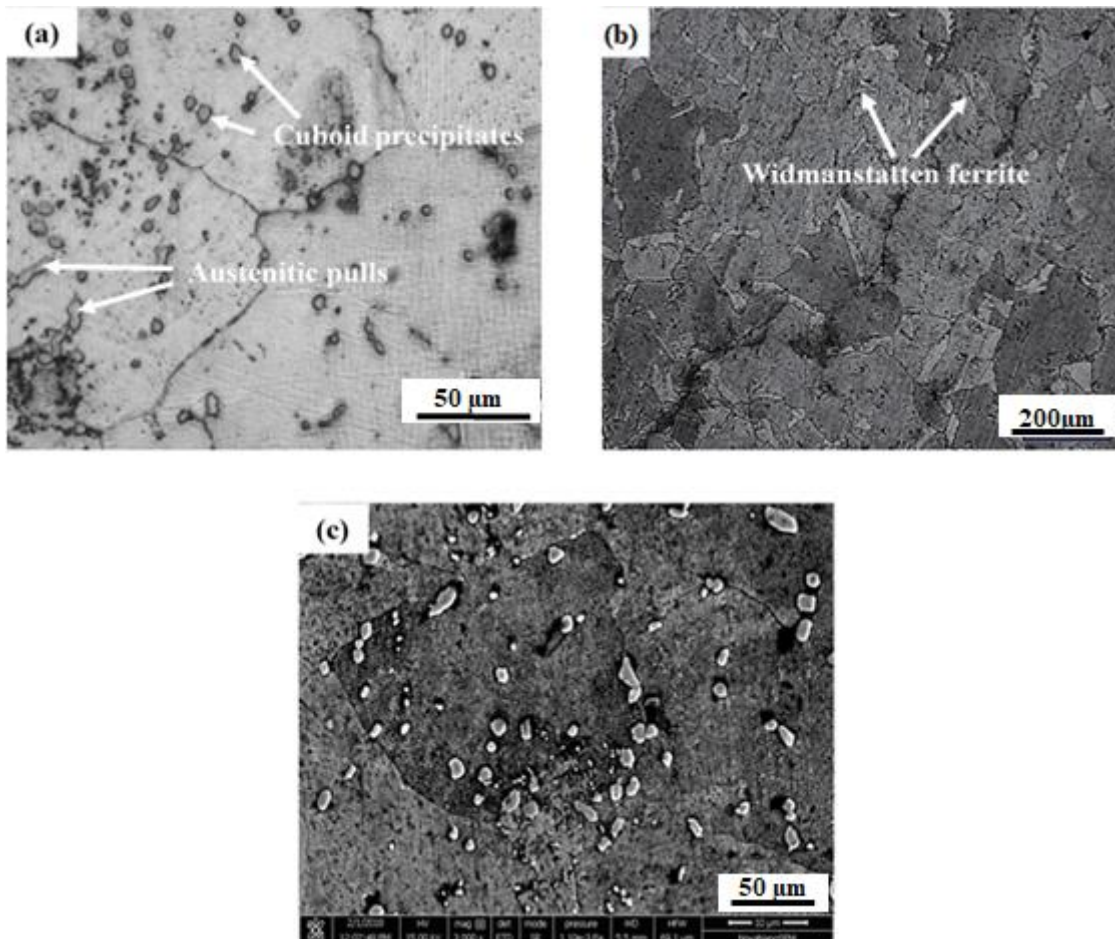

Fig. 3.1: Optical micrograph of (a) as received sample (b) heat-treated at 1200°C and (c) SEM micrograph

Although, some wedge-shaped grains which almost always initiate from the grain boundaries and grow in a particular direction are seen. This can be predicted as Widmanstatten ferrite structure but not martensite. This structure, (Fig. 3.1(b)), is generally seen in ferritic steel with Cr > 17 wt% when cooled below 1140ºC where the austenite typically precipitates at the ferritic grain boundary as Widmanstatten structure [152]. Schaeffler's diagram also supports the statement that according to Cr and Ni equivalent in the material, no formation of martensite takes place and therefore the possible phases will be ~95% ferrite and ~5% austenite.

3.2.2 X-Ray Diffraction and EDS Analysis

The supporting statement is evidenced in X-ray diffractogram analysis. In the as-received condition, the microstructure consists of α-ferrite, Fig 3.2(a). When treated at 1200˚C and air quenched, the presence of austenite (γ) is seen, and also the α-ferrite diffraction peaks become sharp and more intense in Fig 3.2(b).
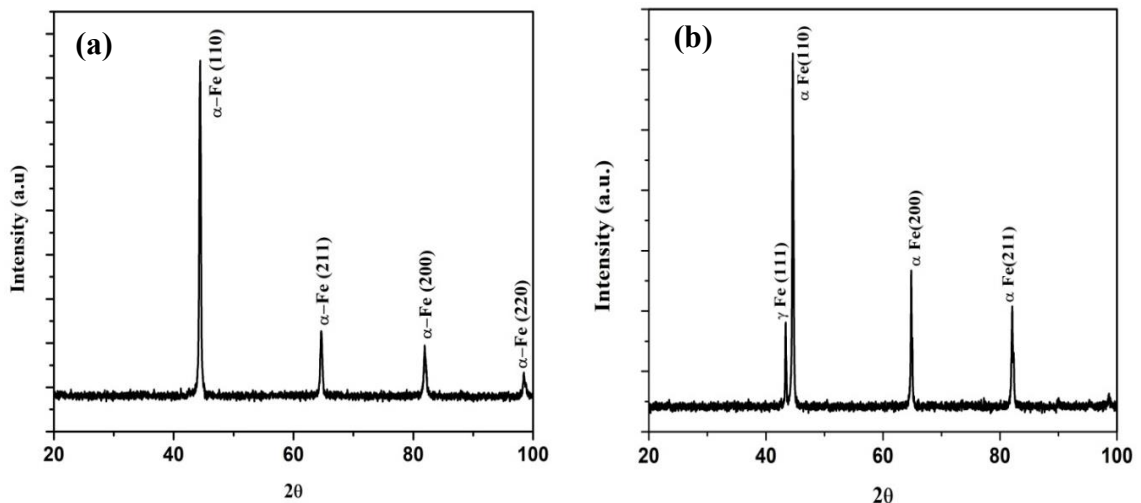

Fig. 3.2: X-ray diffraction pattern of (a) as received and (b) HT at 1200°C.

This indicates that α-ferrite is stable at a given temperature and intensity of diffraction peaks significantly increases. The formation of austenite (γ) is due to the presence of Ni which tends to form γ-phase. This formation of γ-phase increases the solubility of N in Fe-Cr and therefore hinders the formation of precipitate [152]. The possible phases and precipitates that can from during solution treatment are shown in TTT and CCT curve (Fig. 3.3(a, b)). It is clearly seen that sigma phase formation, which is detrimental to the properties of the materials, is formed above 600°C when held at that temperature for a prolonged period of 100 h. Also, the precipitates of carbon and nitrogen are formed much early when held at a temperature above 800°C.
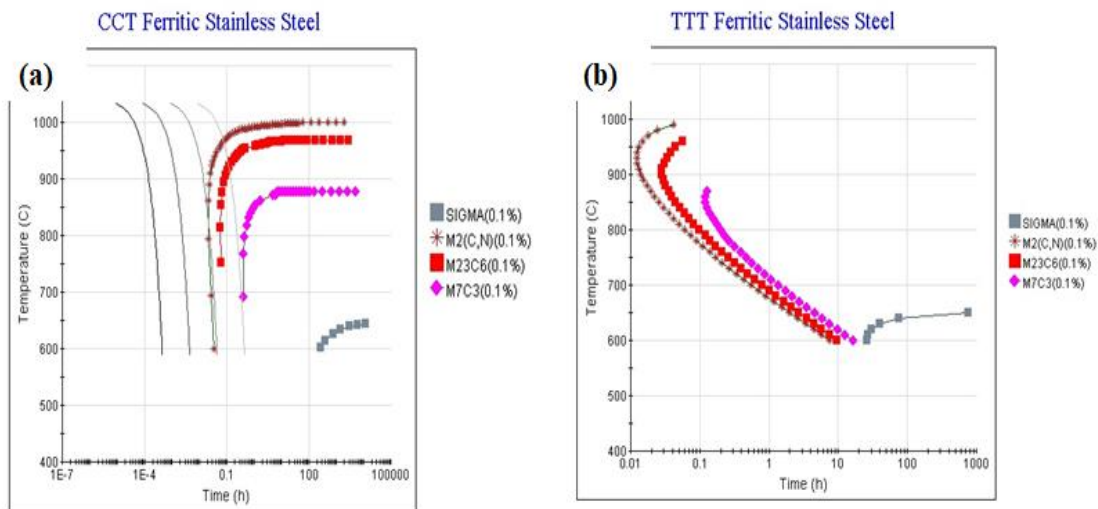

Fig. 3.3: (a) CCT curve and (b) TTT curve for Type 446 Stainless steel

The SEM micrograph of the same samples with EDS analysis (Table 3.1) reveals Cr > 60 wt% as shown in Fig. 3.4. Chromium-rich ferrites with such high chromium could lead to very fine coherent precipitation of chromium-rich phase (bcc α'). It is generally the outcome of the miscibility gap in the Fe-Cr system, and the spinodal type of decomposition. However, a rise in nickel content always discourages such a phenomenon [153].
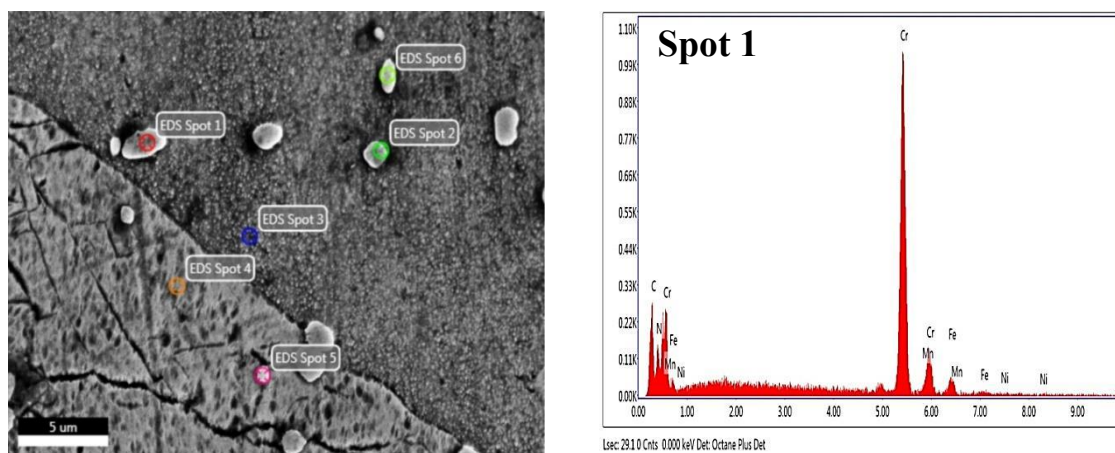
Fig 3.4:. SEM/EDS analysis of secondary phase precipitates

Table 3.1: Elemental data of EDS for base material

Elements	C	N	Cr	Mn	Fe	Ni
EDS Spot 1	13.75	9.38	69.07	1.68	5.43	0.68
EDS Spot 2	13.55	11.46	65.53	2.03	6.96	0.48
EDS Spot 3	17.52	1.92	18.64	1.11	59.95	0.86
EDS Spot 4	16.45	2.23	18.88	1.25	60.20	0.99
EDS Spot 5	15.28	6.71	35.17	0.66	41.69	0.48
EDS Spot 6	12.54	10.22	66.10	1.64	8.88	0.63

TEM image in (Fig 3.5(a)), shows the faceted or polygonal ferritic grains of around ~1-3 μm size. The appearance of the grain indicates that grains are fragmented during processing, and thus they are sharp. Fig 3.5(b) is the bright field image showing a long array of dislocation extending into the grain body. They appear to be originated either at the grain boundary or precipitate matrix interface. Likewise in (Fig 3.5(c)) again it is seen that the precipitate or second phase is quite different in shape. It is a kind of truncated cuboid and a lot of strain field is seen at the interface of the precipitate. The

image in (Fig. 3.5(d)) shows the precipitate or second phase precipitate at the grain boundary. This precipitate is slightly elongated, and the largest dimension varies from 150 nm to 500 nm.
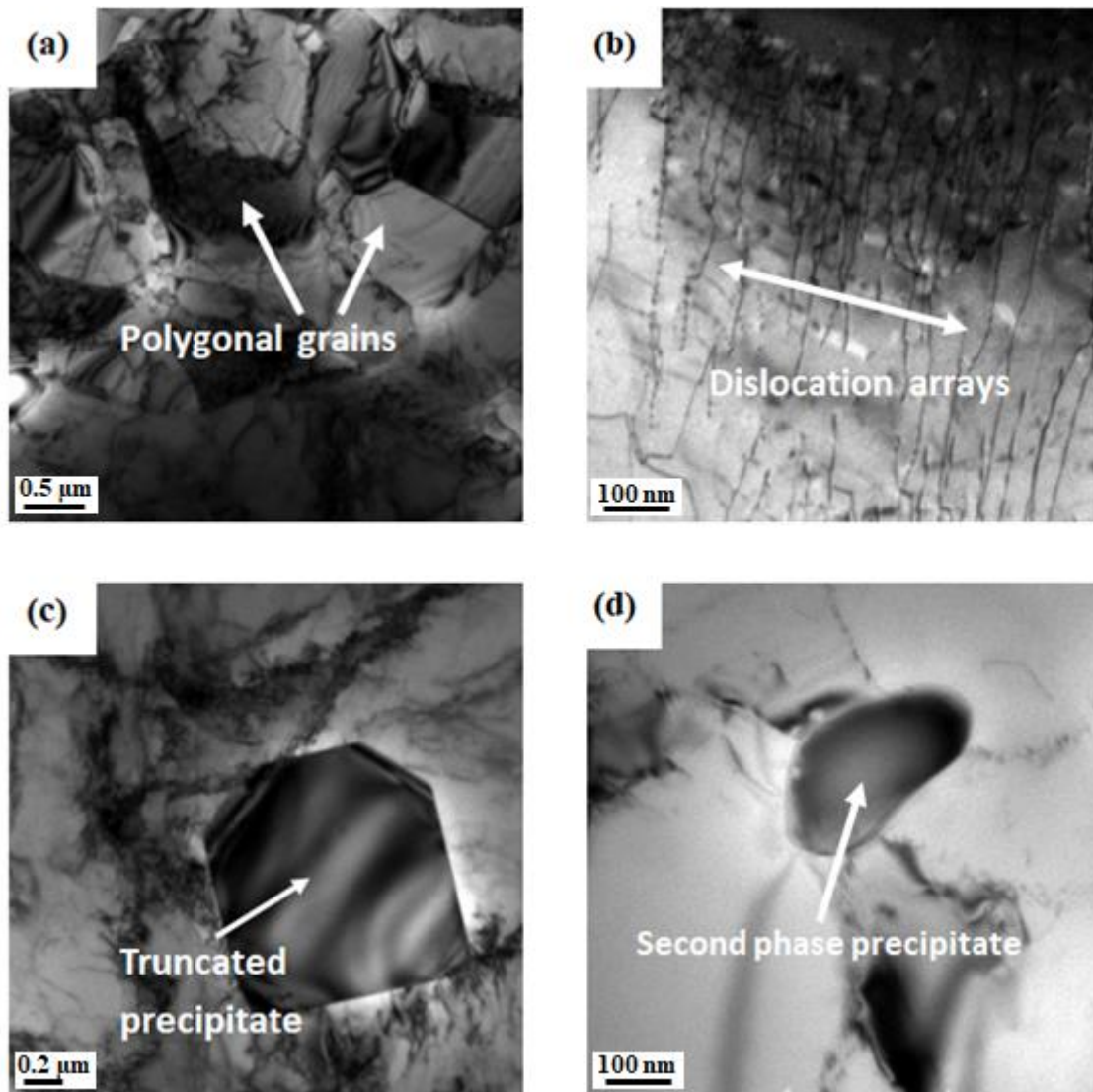

Fig. 3.5: TEM image of received material (a) polygonal ferritic grains (b) arrays of dislocations   (c) truncated cuboid precipitate of the second phase (d) elongated second phase precipitate

3.2.3 Vickers Hardness

The Vickers hardness of the material in as received as well as in heat-treated condition is shown in Fig 3.6. The hardness for as received conditions is 174 HV and increases to 180 HV for 950˚C, whereas with further increase in temperature is observed hardness reaches as high as 193 HV. This change is attributed to the increase in solubility of carbon at higher temperature. Also, dissolution of precipitates in the temperature range of 650˚C to 950˚C when treated for 2 hrs supports the argument [151]. Whereas, with further increase in temperature at 1200˚C, the austenite forms interphase precipitate as Widmanstatten ferrite which may be the cause for increase in hardness to nearly 216 HV.
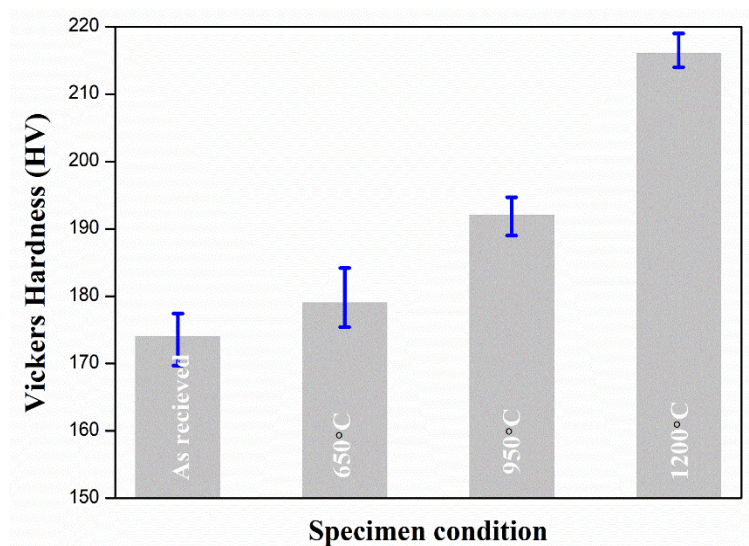
Fig 3.6: The hardness of the specimen under-treated conditions.

3.2.4 Tensile Testing

Summarizing the tensile properties of the specimen, material constants under variable temperatures are given in Table 3.2. Since no extensometer was employed, cross-head displacement (1 mm/min) was taken as specimen extension. The engineering strain-stress curve of the base material is compared under different temperatures in Fig 3.7(a). It is seen that ductility increases several folds when tested at 650⁰C when compared to as-received condition. Also at 350⁰C, serration in the stress-strain curve is

seen which may be the effect of dynamic strain hardening and therefore leads to decrease in ductility. This effect of strain hardening is due to the presence of carbon and nitrogen in the material. These solute atoms diffuse in the specimen at a faster rate than the speed of dislocations to catch and lock them.
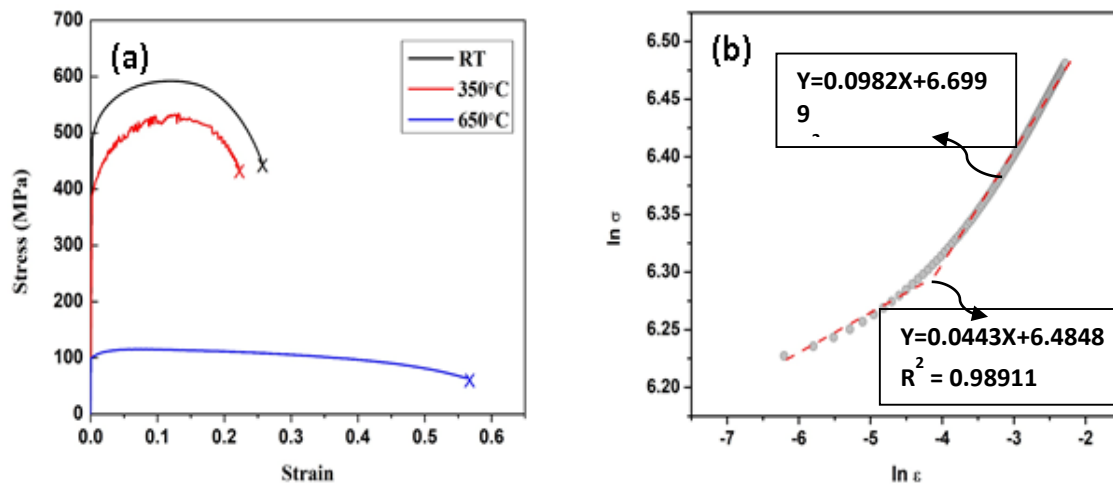

Fig. 3.7: (a) Engineering stress-strain curve and (b) True stress(lnσ) vs. True strain(lnε) plot for the base material at room temperature (RT)

Hollomon power-law relation ($\sigma = k\varepsilon^n$) has been implemented to describe the strain hardening behavior of the specimen, where 'σ' is true stress, 'k' is strength coefficient 'ε' is the true plastic strain and 'n' is strain hardening exponent. To investigate the strain behavior of the specimen, the *log* forms of the true strain-stress curve is shown in Fig. 3.7(b). Non-linearity of '*ln* σ vs *ln* ε' is indicative of two-stage work hardening in different conditions. This can probably be due to the presence of dispersed precipitate within the ferritic matrix of steel which results in a double strain-hardening regime. Kosaka and Funakawa [154] reported that two-stage strain hardening is observed in ferritic steel with fine carbides. The exponent value of the first stage is lower than the exponent value of the second stage. The obtained values are typical with BCC structure having 'n' values between 0.1-0.2. This lower value is because of easiness of cross-slip

causing dislocations not to pile up behind each other [155]. The small difference between YS and UTS is also indicative of lower 'n' values.

Table 3.2: Material constants for the base material in relation to the high-temperature test.

Sample	0.2% YS (MPa)	UTS (MPa)	Work hardening exponent		Strength Coefficient (MPa)		Ductility (% Elon.)
			n_1	n_2	k_1	k_2	
RT	486	589	0.044	0.098	655	812	33
350ºC	392	537	0.056	0.136	572	790	28
650ºC	99	115	0.029	0.062	126	145	67

The fractographic observation of the alloy under the tested condition is shown in Fig. 3.8. The presence of dimples is the key representation of ductile fracture mode. It is well proven that the number of dimples depends on the number of nucleation sites. Large size dimples with uniformity are seen in the sample tested at high temperature as shown in Fig. 3.8(c). These dimples are directionally aligned with their vectors parallel to the applied load vectors. Thereby exemplify the higher ductility to the material.

3.3 ERODENT / SAND CHARACTERIZATION

The physical properties of alumina sand used as abrasive are given in Table 3.3. SEM/EDX of the sand reveals that the particles are angular and irregular shaped with sharp cutting edges as shown in Fig. 3.9(a,b). This is the cause of high mass loss. The erodent particles are found to have an average size of 41.78 μm with the distribution shown in Fig. 3.9(c).
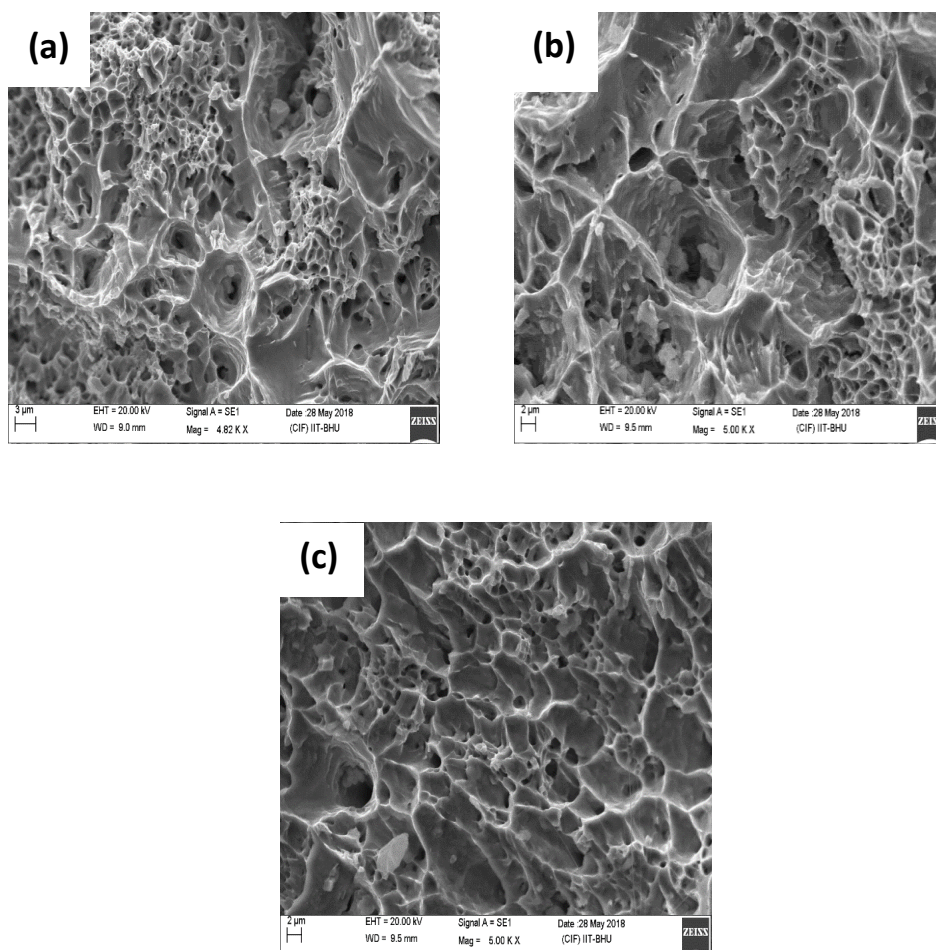
Fig. 3.8: SEM fracture surface of base metal at (a) RT (b) 350°C (c) 650°C.

Table 3.3: Physical properties of Aluminum Oxide erodent

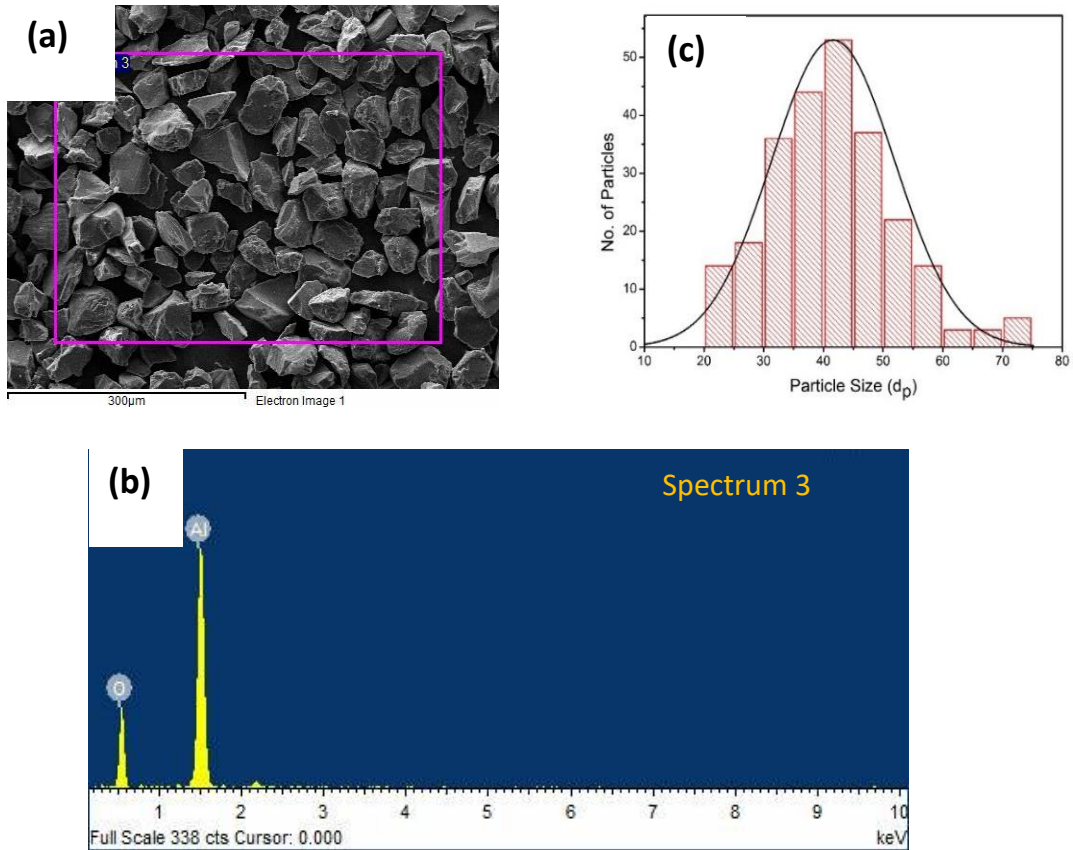| Physical Properties	
Crystal Phase	Alpha
Specific Gravity	3.95 g cm^{-3}
Particle Shape	Sharp, angular
Vickers Hardness	1600 HV
Average particle size	41.78 μm

Fig. 3.9: **(a); (b)** SEM/EDS micrograph; **(c)** Particle size distribution of erodent (Al_2O_3).

3.4 CONCLUSIONS

Following are the conclusions drawn from the present investigation:

1. Microstructure reveals the chromium content in the form of chromium carbides and second phase precipitates which is seen to dissolve beyond 950°C.

2. SEM micrograph shows the precipitation of this second phase on grain boundaries as a needle like structure beyond 1200°C.

3. The hardness of as-quenched samples increases with increasing quenching temperature over the range of 650°C to 1200°C under the influence of the dissolution of precipitates.

4. The presence of C and N creates dynamic strain hardening between RT and 650⁰C and thus decreases the ductility and strain hardening coefficient. However, it increases the work hardening coefficient.

5. The sand particle size distribution shows that the average size of the particle is 41.78 μm. They have a sharp angular shape which is evidenced in the SEM micrograph.